buildings

MDPI

Article

Smart Maintenance and Health Monitoring of Buildings and Infrastructure Using High-Resolution Laser Scanners

Muammer Ozbek

Civil Engineering Department, Faculty of Engineering and Natural Sciences, Istanbul Bilgi University, 80310 Istanbul, Turkey; muammer.ozbek@bilgi.edu.tr

Abstract: An integrated structural health monitoring system was proposed for the rapid assessment of damage on large structures such as high-rise buildings, industrial chimneys, long-span bridges, and similar facilities. The system used ground-based high-resolution IR (infrared) laser vibrometers to measure the dynamic response of structures. To utilize these devices as automated scanners in a fast and efficient way, a new targeting and control mechanism was developed. Different aspects of the proposed system, such as targeting precision and scanning efficiency, were discussed by presenting the results of laboratory experiments and outdoor vibration tests. In addition to the enhancements made in the measurement system, a new methodology was introduced to analyze the recorded vibration response. A novel data processing approach, based on a comparison of the mode shapes calculated on the healthy reference and damaged structures, made it possible to determine the location of the flaw. If available, a finite element model of the analyzed structure also enables the degree of the damage to be calculated very accurately. The reliability of the identification algorithm was demonstrated by conducting extensive numerical simulations and vibration tests on scale building models.

Keywords: damage diagnosis; system identification; vibration response; structural health monitoring; remote measurement systems

Citation: Ozbek, M. Smart Maintenance and Health Monitoring of Buildings and Infrastructure Using High-Resolution Laser Scanners. *Buildings* **2022**, *12*, 454. https://doi.org/10.3390/buildings12040454

Academic Editors: Luca Pelà and Jurgita Antucheviciene

Received: 13 February 2022
Accepted: 1 April 2022
Published: 6 April 2022

1. Introduction

Determining the health condition of structures after natural disasters such as severe earthquakes or hurricanes is essential to ensure safe and effective serviceability [1]. Depending on the type and degree of the observed damage, the structure may be used without interruption, temporarily closed or evacuated, retrofitted, and/or demolished. Structural components are checked in detail by visual examination or by using more sophisticated equipment such as ultrasound and X-ray devices to detect possible problems and risks [2]. However, these operations are very challenging and time-consuming for large structures. Moreover, there will be points that are inaccessible for quick inspection.

With the rapid progress being made in sensor technologies and analysis methods, vibration-based damage detection techniques are increasingly used for structural health monitoring applications [3]. These techniques require the response of the structure to be measured continuously or regularly. Some dynamic properties (natural periods [4], damping ratios [5], mode shapes [6], or wave transmission patterns [7,8]) are designated and tracked as possible damage indicators. Unexpected variations encountered in these parameters can be attributed to damage. Depending on the type of the selected indicator, the damage characteristics (e.g., place and degree) can be determined [9].

Vibration response is commonly measured by accelerometers [10,11], displacement sensors [12,13], inclinometers [14], or strain gauges [15,16] mounted on the structure. Since these sensors require cables to be installed for power supply and signal transfer, they can only be used efficiently at easily accessible locations. However, there may always be points on the structure where instrumentation is very difficult and costly. If the required

sensors cannot be installed at these critical points, the resulting low spatial resolution unavoidably increases the uncertainty in the measurements and limits the reliability of the data obtained [17]. Unfortunately, it is not possible to establish an intensive sensor network and acquire high-resolution (spatial) measurements on large structures such as high-rise buildings, industrial chimneys, or large span bridges.

Non-contact optical measurement technologies, in which measurements are obtained using visible light (photogrammetry, videogrammetry) [18,19] or laser (Doppler interferometry) [20–22], provide new opportunities for measuring the dynamic response of large structures from remote distances of up to 500 m. In laser Doppler velocimetry/interferometry, a laser beam emitted from a source (also called the laser head) is constantly directed to the object being measured. The beam reflecting from the surface of the target is received by the same device. If the object is moving, this generates a difference in the wavelength and phase of the emitted and received laser beams. By using the Doppler principle, the velocity or displacement of the tracked object can be computed with very high precision, even from long distances of up to 500 m. In laser interferometry, velocity and displacement response are calculated directly and the corresponding acceleration is acquired by the post-processing of the recorded data.

Likewise, photogrammetry (also known as videogrammetry) is a well-established and widely used measurement method where the 3D coordinates or deformations of an object can be determined by using 2D pictures taken from different angles and locations. Even though each photographic image only provides 2D information, 3D coordinates and deformations of the structure can be extracted very accurately by the synchronized processing of these images. Velocity and acceleration can be derived manually by analyzing the calculated coordinate information. These methods have recently been used to monitor very challenging structures such as wind turbines or bridges [23,24]. Detailed reviews related to using these promising techniques for health monitoring applications are found in references [25,26].

Since these techniques utilize light to measure the vibrations of a structure, the reflectivity of the surface is the critical parameter that directly affects the accuracy of the data acquired. For long-range measurements especially, the surface of the test object must be treated either by using retro-reflective stickers or by dyeing the surface with special reflective paint, which is approximately 1000 times more reflective than the background material. Although the measurements taken by optical methods are quite promising, their applicability is limited due to the surface treatment requirement.

Ozbek and Rixen [24] successfully utilized a long-range laser Doppler vibrometer to take vibration measurements on a 2.5 MW wind turbine with a rotor diameter and tower height of 80 m. The preliminary tests show that since the blade material has relatively low reflectivity, the intensity of the laser reflecting from the target was not sufficient to acquire accurate measurements. As a surface treatment, the above-mentioned retro-reflective markers (thin, round-shaped stickers with a diameter of 400 mm) were placed on the tower and the blades. It took two licensed turbine climbers (maintenance staff) 6 h to place 55 markers on the structure (11 markers on each blade and 22 markers on the tower). Although the acquired vibration measurements were very accurate, the applicability of the laser Doppler vibrometers for condition monitoring is limited due to the practical problems experienced while placing these stickers on the structure.

This problem is expected to be overcome by the recent developments in IR (infrared) laser vibrometers. Indeed, unlike conventional laser systems using a visible laser beam, IR sensors take very precise measurements and do not require the target to undergo any surface enhancements. Even though this progress alone is quite significant and promising, there are still drawbacks that need to be solved before these systems can be used to efficiently monitor large structures. Unfortunately, current IR laser systems cannot be operated in scanning mode. Conventional vibrometers utilizing visible laser direct the laser beam to the desired spot using the mirrors and lenses that are located inside the laser head. An integrated computer controls the movement of the mirrors and enables all of the

selected target points to be scanned automatically. The size of these mirrors is proportional to the diameter of the laser beam. Since IR lasers have a wider beam diameter compared to visible lasers, they cannot be guided by reflecting or refracting the light beam using the above-mentioned optic controllers.

In order to solve these drawbacks and similar practical limitations, this study aims to develop a new automated IR laser scanner to be used for the rapid assessment of large buildings and infrastructure. The proposed system is expected to be easily applied to existing structures without needing any extensive and costly preparations or installations. Along with the great efficiency and convenience in use, this system provides a very high spatial resolution that is very difficult to attain by using conventional sensor technologies, such as accelerometers and strain gauges.

In addition to the enhancements made in the measurement system, this study also aimed to introduce a new and efficient data analysis method used to determine the location and the extent of possible damage on structures. The identification algorithm developed is easily applied to any finite element models and allows comprehensive damage scenarios involving concurrent damage at multiple locations to be simulated.

Different aspects of the proposed health monitoring system are discussed in the following sections. First, the main features of the measurement method, such as accuracy and scanning efficiency, are described by presenting the results of laboratory experiments and outdoor vibration tests. Then the proposed analysis algorithm is introduced. The accuracy, reliability, and applicability of the developed method are demonstrated by conducting extensive numerical simulations and vibration tests on scale building models.

Within the context of this study, a new guidance mechanism was proposed to overcome the abovementioned control and targeting problems. As shown in Figure 1, the laser head (source) was fixed on a platform that rotates around two axes simultaneously, and is targeted to the desired spot by simply moving the platform rather than by directing the beam with mirrors and lenses.

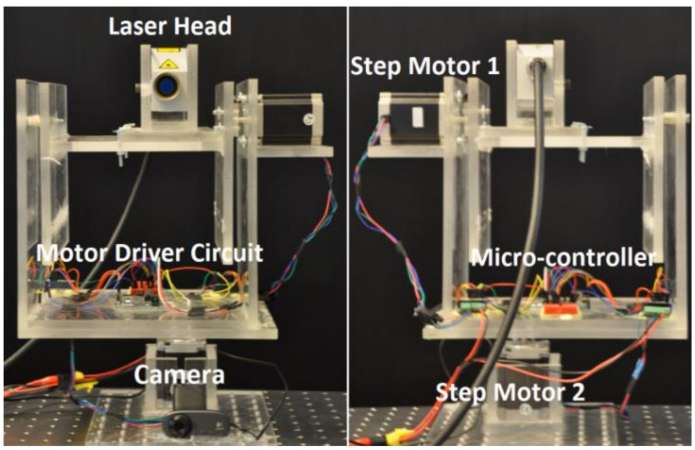

Figure 1. The platform targeting the laser head [27].

Similarly, Figure 2 shows the main components utilized in the measurement setup. A built-in camera system allows the user to observe the test structure through a computer screen. Complicated grid-like profiles can be defined by simply selecting the corner points of the area to be scanned. The spatial resolution can be improved by dividing these forms into the preferred number of sections. The coordinates of all of these points are calculated by a software program that also controls the motion and rotation of the platform. More comprehensive information that is relevant to the operation of the control mechanism, camera calibration, and the corresponding precision is found in recent work by the authors that specifically focuses on the design of the laser scanner [27].

The obtained vibration data were analyzed to investigate whether the dynamic parameters of the structure can be extracted accurately. It should be noted that an accelerometer

was used as a reference during the tests. The vibration response that was acquired by the fixed reference sensor was necessary to scale and colligate the data recorded by the moving sensor (laser spot) at different times.

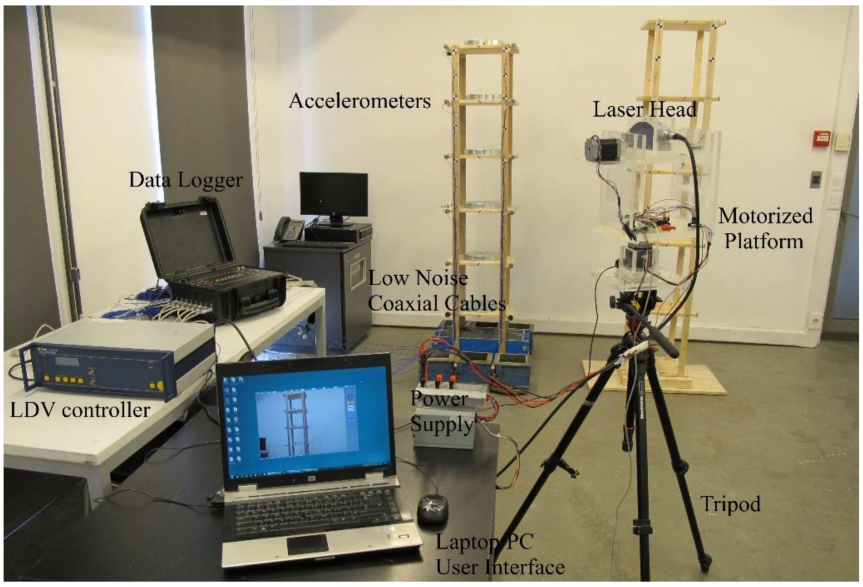

Figure 2. Main components of the measurement system.

Below, Figure 3 shows a comparison of the vibration data acquired by accelerometers and by means of a laser Doppler vibrometer (LDV). The controller of the vibrometer measured the velocity and displacement response. The LDV velocity output was converted into acceleration manually before analyzing these data with those recorded by the reference accelerometers. In the figure, the black and red graphs show the acceleration data obtained by the reference accelerometers. Similarly, the blue graph represents the acceleration calculated by taking the time derivative of velocity measurement recorded by the vibrometer. As demonstrated, the acceleration data obtained by the different methods are in good coherence. The three graphs show the synchronized decaying free vibration response acquired after an impulse-like excitation was applied to the model.

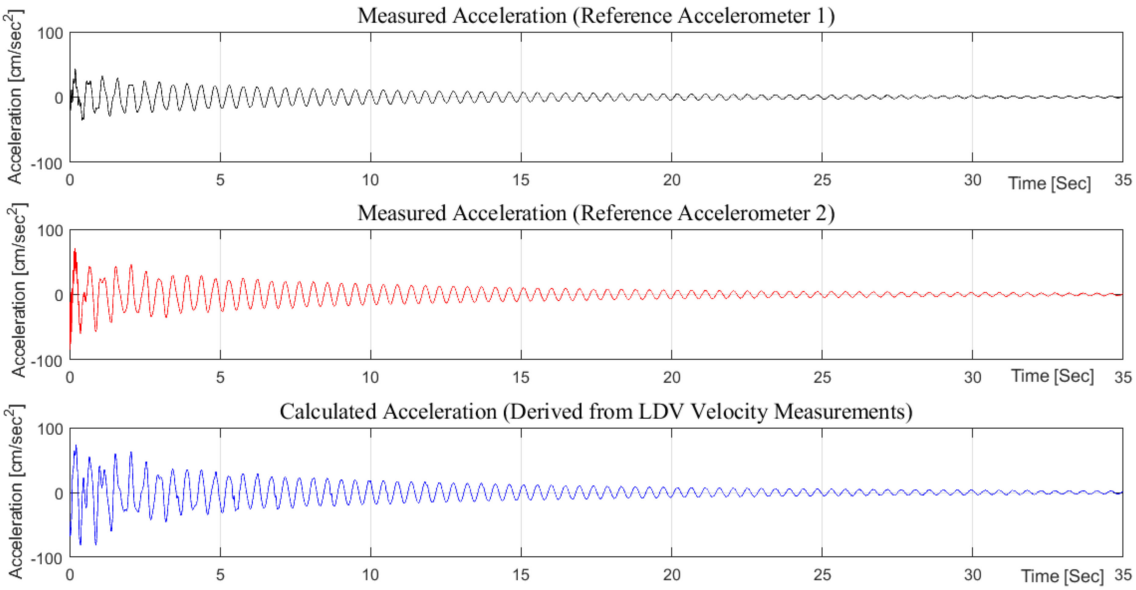

Figure 3. Comparison of the vibration data recorded by accelerometers and LDV.

2. Validation of Efficiency in Scanning Complex Geometries

Following the initial measurements performed in the laboratory, outdoor feasibility tests were conducted to verify the targeting precision. These experiments mainly investigated whether complex geometries are scanned in a fast and effective manner. As shown in Figure 4, the effectiveness of the scanning mode was tested on wind turbine models, which have very challenging and complicated geometries. As a validation test, the laser scanner was programmed to scan the blades of the three turbines successively and then to return to the initial point.

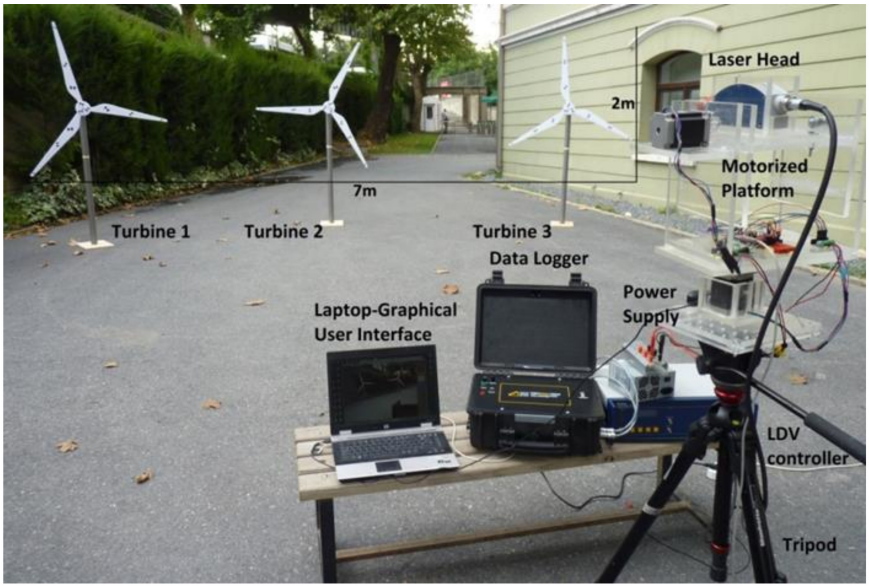

Figure 4. Outdoor tests performed to validate the scanning efficiency [27].

Depending on the prescribed spatial resolution, all of the turbine measurements were completed in 10–15 min. Within this period, nine different measurement paths located in a virtual rectangular area 7 m wide and approximately 2.5 m high, were scanned successively. Once the test was completed, it was observed that the laser spot was very close to the initial target. The difference between the initial and final points was 3–4 mm. The ratio of this deviation to the width of the field of view (4/7000) can be considered to be a dimensionless value representing the accumulated targeting error.

Assuming that the same accuracy is attained while scanning large structures, the accumulated targeting error made for a 100 m high building is expected to be $\pm$6 cm. It should be noted that the reported deviation is not the absolute error made when aiming at the desired spot directly. Instead, this value represents the cumulative error observed when the laser scans multiple points on a path that is 100 m in length and returns to the initial point.

3. The Damage Detection Algorithm

The dynamic analysis methodology developed in this study was based on the well-established mode shape curvature method. This technique compared the mode shapes extracted from the damaged and healthy structures. Since they were used as a reference, it was assumed that the modal parameters of the healthy structure are available beforehand. These parameters are calculated through either some vibration measurements on the structure or the analyses performed on an FE model. This paper does not intend to review the mathematical formulation of the method but instead demonstrates examples of its use in structural health monitoring applications. More comprehensive information that is relevant to the theoretical background of the mode shape curvature method can be obtained through reference articles [28,29].

Within the framework of this project, a new approach that is easily applied to finite element models was introduced. If used only for damage localization, then the method does not involve the use of a finite element model. Depending on the spatial resolution of the measurements, the location of the flaw can be determined precisely by simply comparing the experimentally obtained mode shapes. However, if present, a finite element model makes it possible to understand what the encountered mode shape changes mean and to calculate the level of the damage very accurately.

Since almost all contemporary engineering structures are designed using FE models, it is presumed that these models are available and can be used for structural health monitoring applications whenever needed. FE model-based flaw identification strategies allow comprehensive damage scenarios to be simulated on the structures with irregular geometries and complicated response characteristics [30,31]. Since these techniques utilize previously constructed models, they stand out as time and cost-efficient alternatives for condition-based health monitoring applications.

Current damage detection algorithms are usually based on the continuous tracking of dynamic response parameters. Changes in the natural vibration frequencies and mode shapes are among the most widely used damage indicators [32]. In theory, even a single sensor is sufficient to trace the frequencies and to diagnose whether the structure is damaged or not [33]. However, the location of the damage can only be detected by tracing mode shapes, which requires taking measurements at different points.

The effect of a possible flaw on the mode shape is discussed by presenting the results of damage simulations conducted on the multi-degree-of-freedom (MDOF) structure displayed in Figure 5. For simplicity, lumped mass assumption was used to create an idealized model of a multi-story building with a complicated mass and stiffness distribution. In the figure, J represents the joint number. Similarly, M_i and k_i represent the mass and stiffness of the *i*th story, respectively.

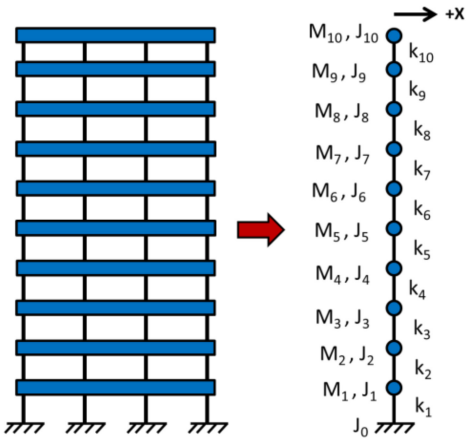

Figure 5. MODF system used in the formulation.

Below, Figure 6 displays how the mode shape changes depending on the position of the flaw. In the figure, the *x*- and *y*-axes show the modal displacement and the number of joints, respectively. The blue and red colors represent the 1st vibration modes of the healthy and damaged structures. The symbol $\phi_{i,1,h}$ represents the displacement of the *i*th joint computed for the 1st mode. The letters *h* and *d* symbolize the healthy and damaged conditions in sequence. Structural damage is represented as a reduction in the stiffness of the selected component (also demonstrated by the red portions on the vertical axis). For the particular case analyzed here, it was assumed that there was damage at the column of the 6th story only, and all of the other columns were considered intact. An extreme state where the damaged element loses 90% of its initial strength was simulated in the formulation. Such a high damage level may not be reasonable in practice and has only been selected to show the differences between the healthy and damaged structures clearly.

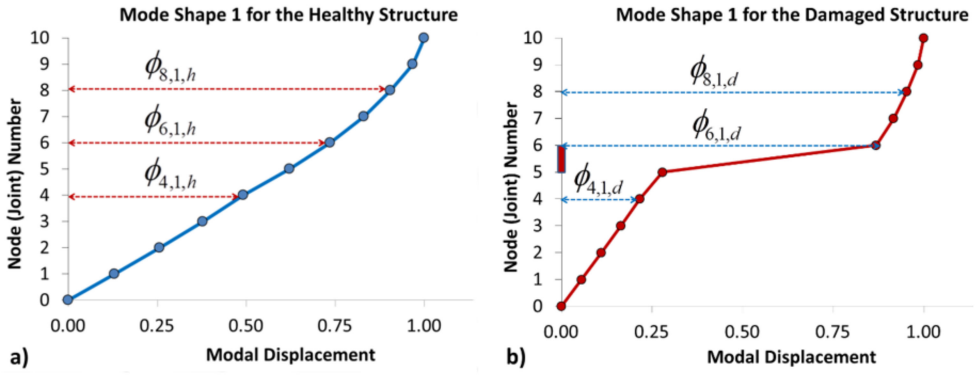

Figure 6. Modal shapes extracted from (**a**) the healthy and (**b**) flawed structures.

As shown in the figure, the inter-story drift calculated for the damaged column is remarkably higher than the displacement of the other stories. In this work, a novel method is proposed to quantify the changes seen in the modal drifts. For this purpose, as shown in Equation (1), a different graph is drawn by selecting data series with coordinates $(x_i;\ y_i)$, where the x_i and y_i values are the modal amplitudes of the ith joint computed for the healthy reference and flawed structure, respectively. In the following steps, this new representation is referred to as *mode shape angle diagram*.

$$(x_i;\ y_i) = (\phi_{i,1,h};\ \phi_{i,1,d}) \tag{1}$$

Once the mode shapes of the healthy structure were extracted, they were stored in a database and used as a reference in the following steps of the analyses. The mode shape calculated from the initial measurement was used as a reference to analyze those obtained from the damaged structure. If the structure was already damaged when the initial (reference) measurement was taken, the analyses show how the flaw has changed relative to the initial damage state. However, if a validated FE model exists, the modes extracted from the model can be used directly as a reference. In this case, all of the measurements (including the initial one) can be compared to the modes of the FE model, making it possible to extract the damage characteristics of the initial measurement as well.

Following the calculation of the reference modes, consecutive damage simulations were conducted by generating structural flaws on some selected elements. The damage was characterized by a decrease in the stiffness of these particular components. The stiffness of a load-resisting element was formulated by Equation (2). In the equation, the letters E, I, L, and k denote the elasticity modulus of the material, the moment of inertia of the cross-section, the length of the member, and the corresponding stiffness value, respectively. In this study, the modulus of elasticity, denoted by E, was used as the control variable to represent the damage to the system.

$$k \propto \frac{E\ I}{L^{\,3}} \tag{2}$$

The flowchart followed in the analyses is shown in Figure 7. It should be noted that the proposed methodology was based on two different analysis loops, namely, the member/story-based and system/structure-based loops, which are shown by the red and blue colored arrows, respectively. The steps displayed in the figure are explained in more detail in the following sections. A repetitive damage simulation was performed by gradually decreasing the elasticity modulus. The damage level was characterized by a % loss in the stiffness and is formulated by Equation (3) as follows:

$$\%\ \ DamageLevel = \left(1 - \frac{Stiffness_{\ damaged\ member}}{Stiffness_{\ healthy\ member}}\right) \times 100 \tag{3}$$

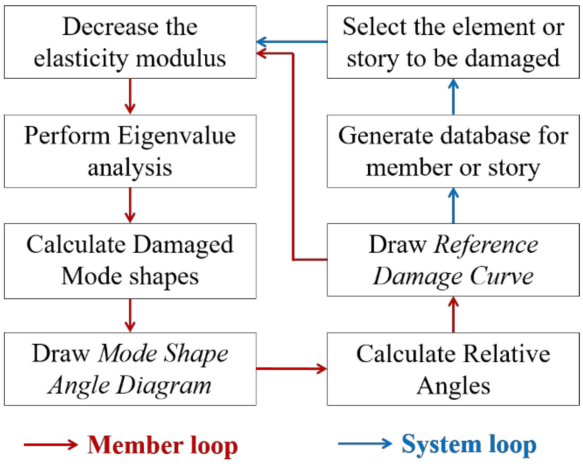

Figure 7. The methodology followed in the damage simulations.

At each step of the simulation, eigenvalue analysis was conducted, and the corresponding modal parameters were extracted. The mode shape computed for the damaged structure was then used to draw a *mode shape angle diagram*, as described by Equation (1). Below, Figure 8a displays the *angle diagrams* produced for the healthy reference (in blue) and for the damaged structure (in red). The healthy reference can also be examined as a damaged building with 0% damage. When Equation (1) is applied to the reference, $\phi_{i,1,h}$ is equal to $\phi_{i,1,d}$ for all the stories. The corresponding diagram is simply the graph of $y = x$, and forms an angle of 45° with the x-axis. Therefore, the slope is constant and equal to 1 for all of the members along the blue graph.

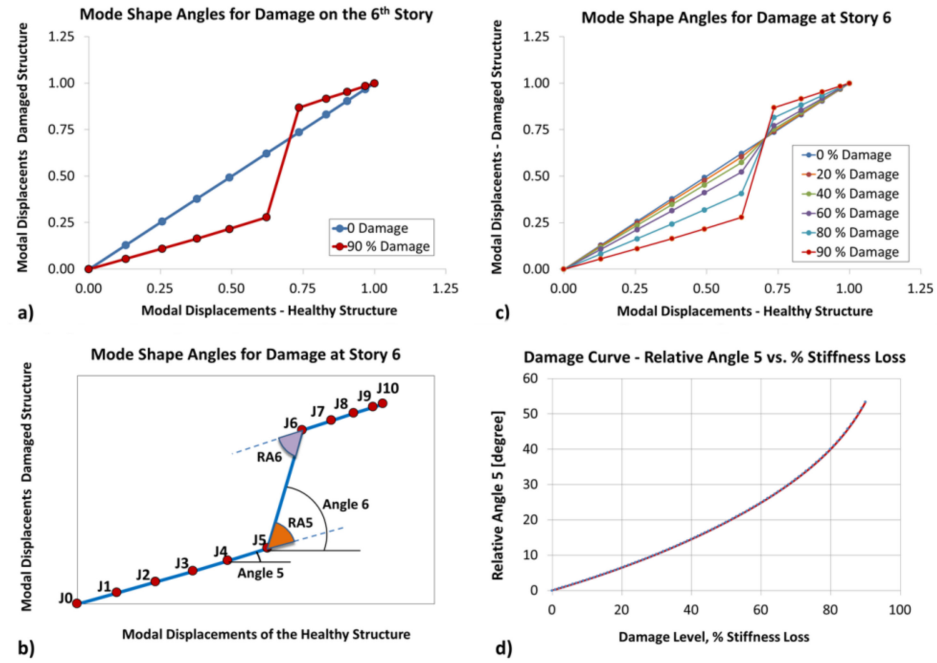

Figure 8. The mode shape variation analysis with respect to damage location. (**a**) damage effect on mode shape angle (**b**) angle notation used in the analyses (**c**) increase in the angle depending on the damage (**d**) reference damage curve.

On the other hand, the red diagram obtained for the damage scenario, where the 6th story loses 90% of its initial stiffness, shows that the slopes of the line segments change abruptly at the lower and upper joints of the damaged component, namely at joint 5 and 6. However, it can be seen that the slopes of the segments do not change at the joints of

the healthy stories. For instance, the slope of the first five segments representing stories 1–5 is the same. Similarly, there is no variation in the slopes of segments 7–10. This article introduces a new approach for interpreting this observed pattern.

The notation utilized in this study is displayed in Figure 8b, which consists of 11 joints (J_0 represents the foundation) and 10 segments (stories). Once the mode shape angle diagrams were obtained, the angle between each line segment and the horizontal axis was computed individually. The angle between the *i*th segment and the horizontal axis was called as $Angle_i$ and was calculated using Equation (4).

$$Angle_{\ i} = \text{atan}\left(\frac{\phi_{i+1,1,d} \ - \ \phi_{i,1,d}}{\phi_{i+1,1,h} \ - \ \phi_{i,1,h}}\right) \tag{4}$$

Similarly, the difference between the angles of the successive stories i and $i+1$ is referred to as the *Relative Angle*$_i$ and is represented by the symbol RA_i and calculated by using Equation (5):

$$RA_{\ i} = Angle_{\ i+1} - Angle_i \tag{5}$$

As mentioned before, if the $(i+1)^{th}$ member is healthy, the angle between segments i and $i+1$, RA_i is equal to zero. However, in case of a possible flaw, this difference increases significantly depending on the extent of the damage. Figure 8c shows how *mode shape angle diagrams* and *the relative angles* change with regard to the damage level or % stiffness loss. It should be noted that Figure 8c shows the variation in the diagrams for several scenarios where the 6th floor experiences stiffness losses ranging between 0% and 90%. During these successive analyses, *relative angles* were calculated for each damage level separately and then used to calculate the *reference damage curve* shown in Figure 8d. In the figure, the x and y axes display the % *loss* in the story stiffness and the resultant *relative angle* in sequence.

Damage levels resulting in a stiffness loss of 90% may not be reasonable in practice. These extreme cases were analyzed to show more clearly how the variation in the mode shape (and the relative angle) depends on the damage level. Possible structural flaws are expected to be detected much earlier, before they reach such critical levels and cause irreversible structural problems.

The proposed method does not involve utilizing a finite element model to appoint the location of the flaw. Mode shapes can also be calculated by performing dynamic tests on healthy and damaged structures. Comparing these experimentally obtained mode shapes are sufficient for diagnosing possible damage and for accurately determining its location. However, an FE model is needed to comprehend what the encountered mode shape variation means and to estimate the degree of the flaw. Since all modern engineering structures are designed using FE models, it is presumed that these models already exist and can be used for damage identification purposes whenever required.

4. Damage Simulations and Analyses on a 15-Story Residential Building

The mathematical accuracy of the proposed technique and the consistency of the damage estimations (e.g., location and extent) were initially verified on an FE model. This approach eliminated possible sources of error and uncertainty that could be attributed to the measurements. It also enabled the critical analysis variables to be controlled accurately.

The efficiency of the utilized identification method was validated using the finite element model of the 15-story residential building shown in Figure 9 below. The model was prepared using the SAP2000 program. The structure had four bays in both the x and y directions. The length, width, and height of the building were 20 m, 16 m, and 45 m, respectively. The structural plan consisted of six different column cross-sections, and each was represented by a different color in the figure. For simplicity, a fixed-base foundation assumption was used. In addition, separate rigid diaphragms were defined for each story.

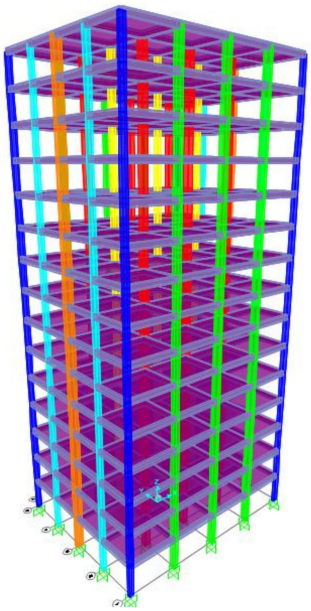

Figure 9. The FE model of the multi-story residential building used in the analyses.

To determine the mode shape used as a reference for the later steps in the simulations, an eigenvalue analysis was first conducted on the healthy structure. The major vibration modes and the corresponding natural periods are summarized in Table 1.

Table 1. Vibration modes and natural periods.

Mode Number and Direction	Natural Vibration Period (s)
1st mode in X Direction	1.68
1st mode in Y Direction	1.53
1st Torsion	1.44
2nd mode in X Direction	0.55
2nd mode in Y Direction	0.50
2nd Torsion	0.48

Some of the extracted vibration modes (the 1st and 2nd modes in the X direction and the 1st torsion mode) are also shown in Figure 10. It should be noted that in the figure, the scale factors of the modal displacements were intentionally increased to make it easier to visualize how the building deforms in these modes. The first mode in the X direction was used as the reference state in the analyses.

One of the main objectives of the analyses described in this section was to check whether the proposed algorithm was able to identify concurrent damage on several stories. Therefore, in order to simulate complex damage scenarios, four different stories (2, 5, 9, and 13) were damaged concomitantly.

For the initial steps of the analyses, simple damage cases with damage on only a single story (e.g., at 2nd story) were considered. At this preliminary stage, the 14 remaining stories were presumed to be intact. The stiffnesses of the columns on the damaged story were gradually decreased with a step increment of 1%. Next, eigenvalue analysis was performed; the corresponding mode shapes were calculated and processed as described in Figure 7. Once all of the damage levels from 0% to 80% were simulated successively, the *damage reference curve* was drawn for this particular story and stored in a database to be used for further simulations. The above-mentioned analysis was repeated for all of the stories separately until the damage response characteristics of the structure had been completely determined. The damage curves obtained for four different stories (2, 5, 9, and 13) are shown in Figure 11 below.

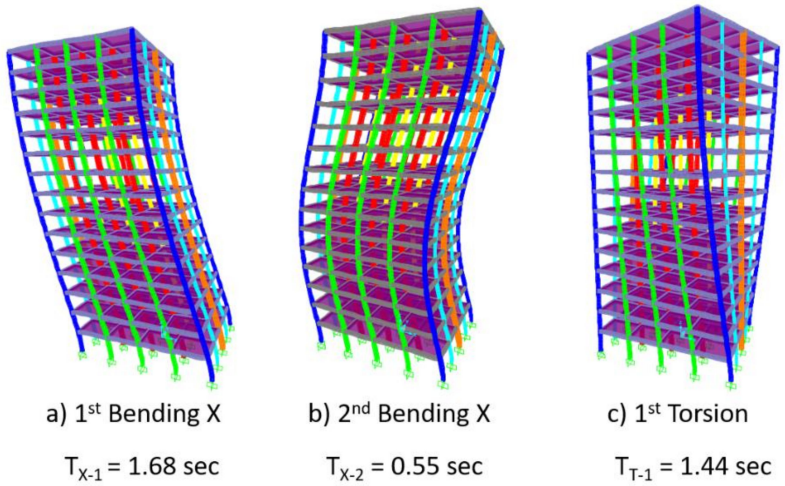

Figure 10. Vibration modes and periods of the analyzed system (**a**) the 1st bending mode in X direction (**b**) the 2nd bending mode in X direction (**c**) 1st torsion mode.

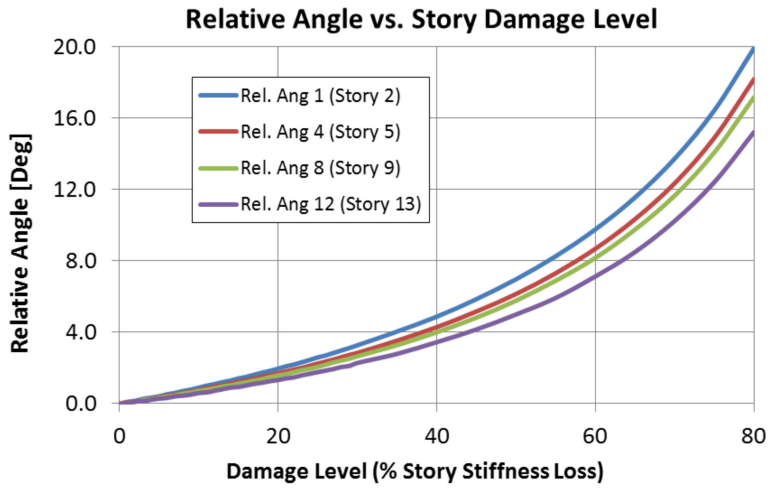

Figure 11. Reference damage curves obtained for several stories.

It should be noted that these curves were obtained by considering the damage incurred to a single story at a specific time. For example, in Figure 11, *relative angle 1* represents the health condition of the 2nd story. Similarly, *relative angles* 4, 8, and 12 are damage indicators for the 5th, 9th, and 13th stories, respectively.

In order to utilize these *damage curves* as a reference for more complicated scenarios involving concurrent damage on several floors, it should first be confirmed whether the damage indicators were affected by the damage on other stories. This verification is achieved by monitoring how the damage indicator of a particular story changes if other stories are also damaged concomitantly. The results of these simulations are presented below in Figure 12. The figure clearly proves that the *relative angle* computed for a particular story is not sensitive to the damage in different parts of the structure. For instance, Figure 12a shows the variation in *relative angle 1* for different damage cases. It shows that the angle obtained for a case where only the 2nd story is damaged is exactly the same as the angle determined for a case where there were flaws on two (e.g., 2nd and 5th) or even on all four different stories (2nd, 5th, 9th, and 13th) at the same time. The results of the analyses definitely disclose that *relative angle 1* is sensitive to the current state of the 2nd floor only. The same tendency is also seen for the damage indicators of other floors. It should be noted that there can be some very slight deviations between the relative angles that have been computed for the single-flaw and multiple-flaw scenarios for very high damage levels (e.g., 70–80% stiffness losses). However, as mentioned previously, such extreme damage cases

were modeled to see the limits of the identification algorithm, and they are not realistic in practical applications.

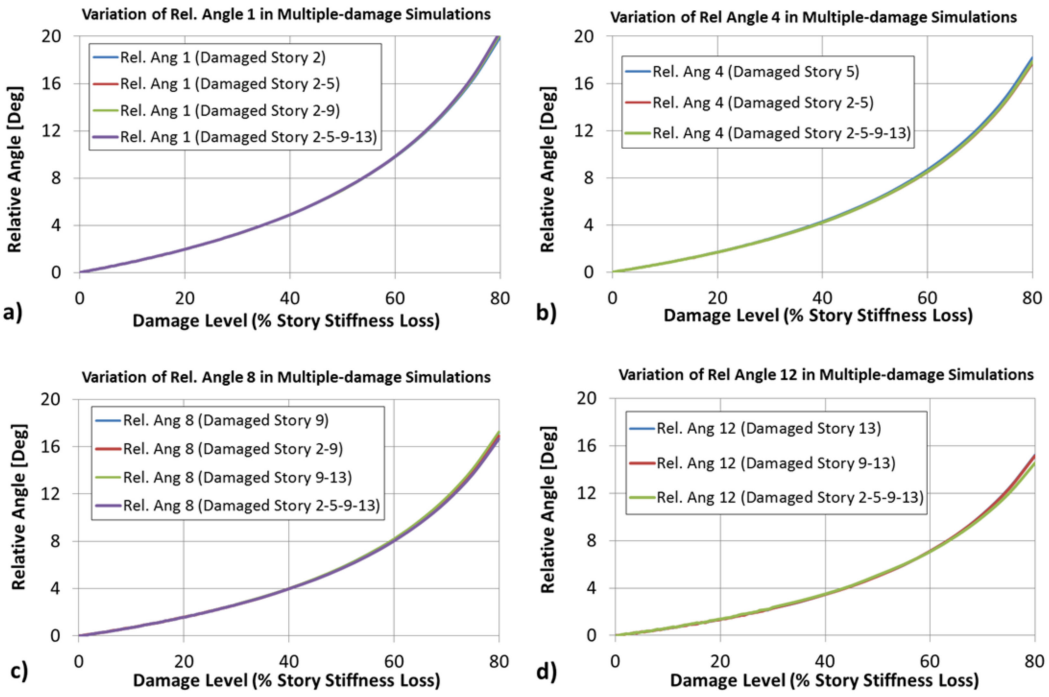

Figure 12. *Relative angles* calculated during concurrent damage on different floors (**a**) *rel. ang.1*, (**b**) *rel. ang.4*, (**c**) *rel. ang.8*, (**d**) *rel. ang.12*.

The verification of the fact that a damage indicator was only sensitive to the current state of a particular story made it possible to superimpose the effects of flaws observed in different parts of the structure simultaneously. In this way, the instantaneous health condition of each floor was analyzed individually by decomposing a single mode shape extracted from a scenario representing concurrent damage at several points.

In order to show the efficiency of the proposed technique when analyzing intricate damage patterns, a case where four different stories (2, 5, 9, and 13) were damaged concomitantly was analyzed. The stiffnesses of these floors decreased by 25–40% when the elasticity moduli were adjusted to prescribed values. The mode shape of this structure was calculated by eigenvalue analysis and compared with the mode of the healthy reference, as described previously. Table 2 below shows the comparison of the prescribed and calculated damage levels. The table shows that the estimations are very close to the pre-determined damage levels. The degree of the damage was estimated very accurately, showing a maximum error rate of 3.4%. The values in Table 2 are also shown in Figure 13.

Table 2. Prescribed and calculated damage levels.

Damaged Story	Pre-Scribed Stiffness Loss %	Damage Index	Calculated Angle (Deg)	Calculated Damage %	Error
2	15	RA_1	1.46	15.41	2.7%
5	25	RA_4	2.23	25.15	0.6%
9	40	RA_8	4.20	41.34	3.4%
13	20	RA_{12}	1.43	20.58	2.9%

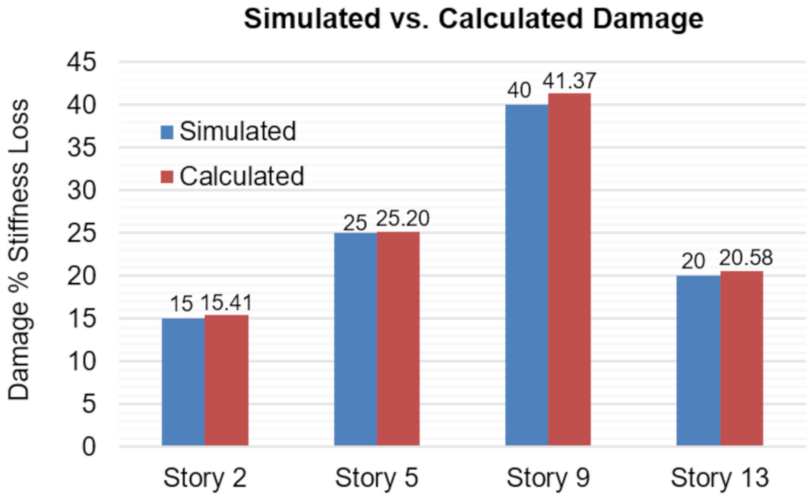

Figure 13. Comparison of prescribed and calculated damage levels.

5. Damage Detection Tests Performed in the Laboratory

Analyses conducted on the numerical models are essential to eliminate possible sources of uncertainty due to measurement errors. Once the theoretical limits of the identification algorithm are known, the experimental results can be interpreted more clearly. Following the simulations performed on the FE model, dynamic tests were also carried out on the scale model shown in Figure 14 to understand the difficulties that are encountered during practical applications. As seen in the figure, a representative FE model was also constructed for the abovementioned damage simulations. The wooden test structure had six stories and a total height of 1800 mm. The columns had rectangular cross sections with dimensions of 40 × 10 mm. A 20 mm thick wooden plate that was 300 × 400 mm in size was used to represent the slab connecting the columns. The modulus of elasticity value of the wood was calculated as 630 MPa by performing bending tests on the columns. Metal blocks weighing 10 kg were fixed at each story. The model was firmly connected to a wooden base plate. As displayed in Figure 2, 200 kg weights were placed on this plate to provide stability.

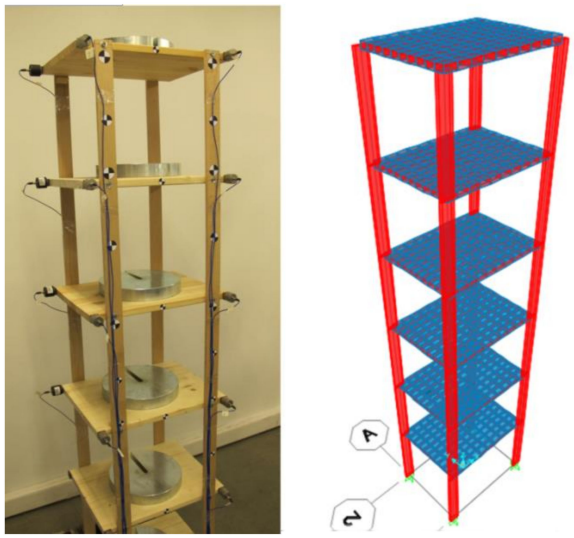

Figure 14. Building models tested in the lab and the corresponding FE model.

Although one fixed reference sensor was sufficient to scale the laser measurements, 16 accelerometers were placed on the structure for validation tests, as shown in Figure 14.

The PCB-393B04 model vibration sensors used for these tests were sensitive to low-frequency oscillations and had a bandwidth of 0.06 Hz to 450 Hz [34]. The mode shapes calculated using 16 accelerometers were utilized to check whether the modal parameters extracted from accelerometers and laser measurements were consistent or not. During the tests, laser measurements were taken every 50 mm. Since the vertical distance between accelerometers (story height) was 300 mm, it was concluded that the laser measurements provided a spatial resolution that was six times higher compared to the accelerometers. The modal parameters calculated through these dynamic tests and analyses are presented in Table 3. Some of dominant vibration modes are also shown in Figure 15. The analyses performed in this work is based on the 1st mode in Y direction.

Table 3. Dynamic properties calculated for the test model.

Vibration Mode	Period (s) SAP2000	Period (s) Experimental	Damping Ratio (%) Experimental
1st Mode in Y Direction	0.746	0.746	2.95
1st Mode in X Direction	0.302	0.299	2.52
2nd Mode in Y Direction	0.214	0.213	1.93
1st Torsion	0.168	0.168	2.37
3rd Mode in Y Direction	0.103	0.110	2.09
2nd Mode in X Direction	0.060	0.076	1.64
4th Mode in Y Direction	0.061	0.069	1.73

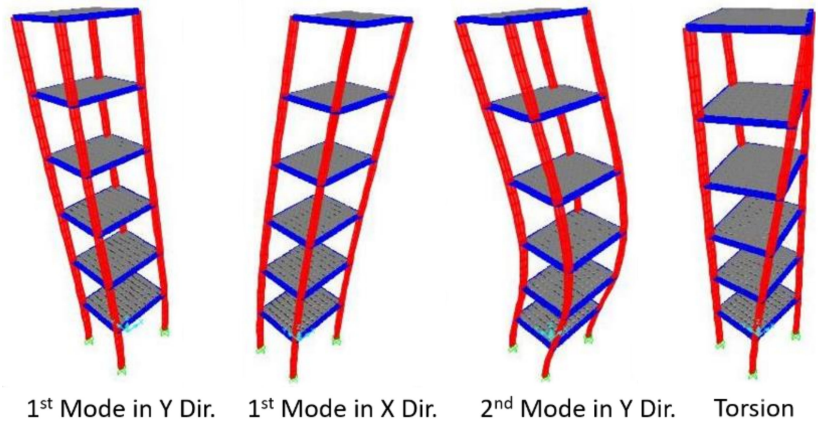

Figure 15. Vibration modes extracted for the model.

As shown in Table 3, the eigenfrequencies obtained from the experimental analyses and the SAP2000 model are very close. The utilized FE program allows the user to scale the bending and torsional properties of the members separately. In this way, the FE model is calibrated very easily using the experimental data without having the exact stiffness properties of the column–plate connection. Since the analyzed model is perfectly symmetrical with respect to both axes, the dominant modes are mostly uniaxial and uncoupled. Therefore, the stiffness scaling coefficients are easily obtained by trial and error for each direction independently. Torsion mode is the only coupled mode, but the torsional rigidity is directly controlled by a separate scaling coefficient until the experimental and numerical periods are the same. However, vibration modes are generally expected to be coupled for complex buildings with irregular geometries. If the dominant modes have components in the x and y directions simultaneously, advanced optimization tools are required to calibrate the model before starting the damage simulations.

Model validation and optimization techniques are beyond the scope of this study. However, since almost all contemporary engineering structures are designed using FE models, it is presumed that validated FE models are already present and can be used for structural health monitoring applications whenever needed.

Once the mode shapes representing the healthy reference were obtained, all of the columns on the 2nd and 4th stories of the model were damaged by cutting them with a saw. Initially, the columns had 40 × 10 mm rectangular cross-sectional areas. Using an adjustable saw, the short sides of the 2nd and 4th story columns were cut at depths of 1 mm and 2 mm on both sides, respectively. The damaged columns were expected to have cross-sections of 38 × 10 and 36 × 10. The most significant problem at this stage was quantifying the damage incurred on the columns. The % of residual stiffness of the damaged component was calculated by taking the ratio of the moment of inertia values of the damaged and healthy structures as shown in Equation (6).

$$\%\ \ Residual\ \ Stiffness = \left(\frac{I_{damaged}}{I_{healthy}}\right) \times 100 \tag{6}$$

In Equation (6), I represents the moment of inertia of the element. For a rectangular cross-section with a width of b and height of h, I can be calculated as follows:

$$I = \frac{1}{12} bh^3 \tag{7}$$

By substituting Equation (7) in Equation (6), a new formulation showing the change in the *% residual stiffness* with respect to the *depth of cut* can be written as

$$\%\ \ Residual\ Stiffness = \left(\frac{h_1 - d}{h_1}\right)^3 \times 100 \tag{8}$$

Using Equation (8), the stiffness losses at the 2nd and 4th stories were calculated as 14.3% and 27.1%, respectively. The above-mentioned dynamic analyses were conducted, and the mode shape of the damaged structure was calculated. Then, the damage parameters (location and extent) were estimated by performing simulations on the FE model shown in Figure 14 by following the procedure in Figure 7. The calculated and estimated damage levels are summarized in Table 4. It can be seen in the table that the damage level was predicted with a maximum error of 19.4%. This error is greater than the maximum value reported in Table 2 (3.4%). This difference is attributed to the difficulties in quantifying the degree of the flaw rather than the efficiency of the method. It can be concluded that damaging a component physically is not a fully controllable process and that cutting the columns with a saw always damages the elements more than intended. Wood, the material that the building model is made of, is not a homogenous material. The wood knots or micro-cracks may cause the columns to have different mechanical properties. On the other hand, even an error of 19–20% can be considered to be satisfactory. This accuracy is high enough to diagnose possible structural damage and to take measures at early stages.

Table 4. Results of the damage analyses.

Column Segment	Calculated Damage Stiffness Loss (%)	Estimated Damage Stiffness Loss (%)	Estimation Error
10 (the 2nd story)	14.26	16.09	12.8%
20 (the 4th story)	27.1	32.37	19.4%

The dynamic tests performed on the model also enabled the location of the flaw to be determined accurately. As mentioned previously, the spatial resolution of the laser measurements was 50 mm, resulting in 36 segments in total. As mentioned previously, the columns were damaged at two different locations, namely at segments 10 and 20, which were on the 2nd and 4th stories, respectively. On each story, all four columns were damaged at the same locations. The results of the analysis performed to find the location and extent of the flaws are shown in Figure 16 below. In the figure, the x axis represents the segment number. Similarly, the y axis displays the damage in % of stiffness loss.

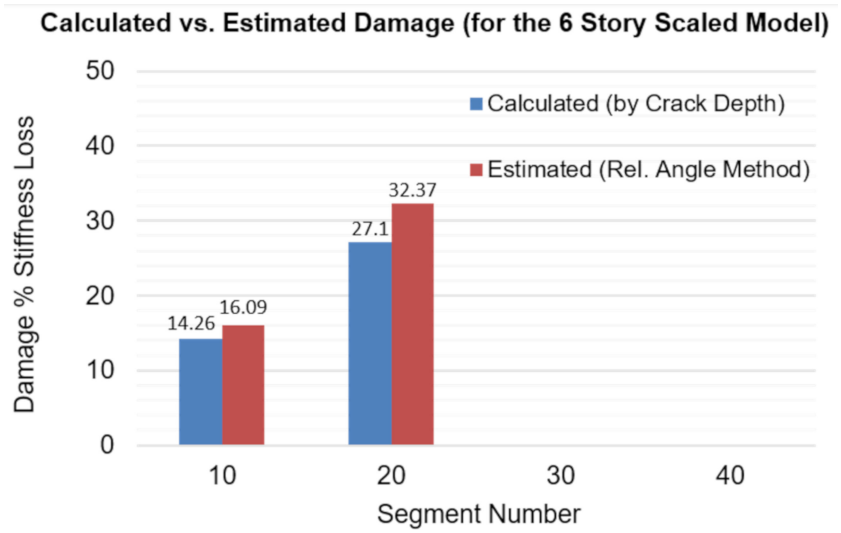

Figure 16. Location of the damaged column segments.

6. Applicability of the Proposed System for Testing Large Structures

The system developed in this work used an IR laser beam to measure the dynamic response of the structures. If the tests are conducted in the daytime, it is unavoidable that the system will be exposed to sunlight, which is a major source of IR light. Hence, it is essential to validate whether the sun and other similar light sources affect the accuracy of the measurements. The vibrometer described in this work generated a laser beam with a specific wavelength (1500 nm). The beam reflecting from the target is received and analyzed by the same device. An integrated band-pass filter only allows light beams with a wavelength of 1500 nm to reach the receiver. In this way, noisy signals from the surrounding environment are eliminated. Conventional IR vibrometers are mostly guaranteed (by the manufacturers [35]) to provide very accurate measurements in almost any weather conditions, except for in some extreme cases such as rain or heavy fog.

The health monitoring system proposed in this study can take measurements from any location and orientation. The IR light emitted from the source does not need to be perpendicular to the target surface. Independent from the angle between the beam and the surface, Doppler vibrometers always measure the vibration in the direction of the laser beam. However, the angle of incidence should be known to decompose the measured vibration into the corresponding axes.

Below, Figure 17 shows the calculation of the coordinates and the reflection angles for several measurement points. In the figure, the laser vibrometer is assumed to be placed at the center of the coordinate system. If possible, taking the measurements from the same location on the ground facilitates the comparison of the data acquired at different times. The initial orientation of the laser vibrometer corresponds to the z-axis. In Figure 17, Points A and B show the initial and final measurement points on the structure, which are represented by the position vectors $\vec{r}_1$ and $\vec{r}_2$, respectively. The vertical angles between these position vectors and the horizontal plane are represented by β_1 and β_2. Similarly, the symbols α_1 and α_2 denote the angle between the z-axis and the projection of the position vectors on the ground plane. The step counters of the two motors used to rotate the platform around the x and y axes acted as a digital protractor. They measured the horizontal and vertical angles (α and β) for every test point with an accuracy of 0.014o, and these values were stored in the memory for further calculations. If required, a separate device, such as a theodolite or total station, can be used for this purpose as well. The guidance mechanism of the system also includes a laser range finder that is measured to find the distance ($\left|\vec{r}_1\right|$ and $\left|\vec{r}_2\right|$) between the laser vibrometer and the measurement points A and B.

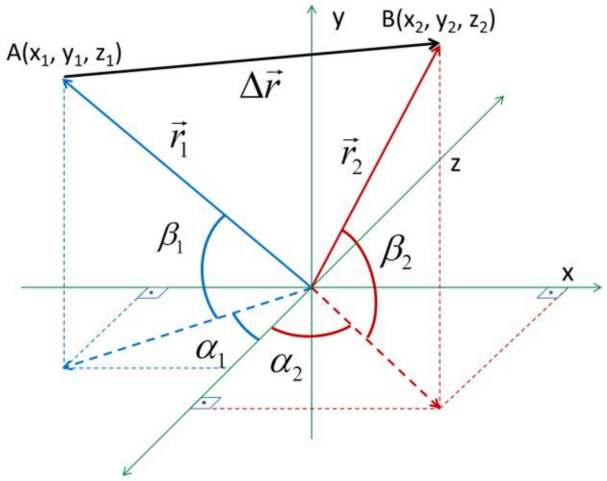

Figure 17. Calculation of the reflection angles [27].

Using the distance and the angles α and β, the 3D coordinates of the initial and final points can be calculated. The overall displacement vector drawn between these points is formulated as shown via Equations (9) and (11).

$$\Delta\vec{r} = \vec{r}_2 - \vec{r}_1 \tag{9}$$

$$\Delta\vec{r} = (x_2 - x_1)\,\vec{i} + (y_2 - y_1)\,\vec{j} + (z_2 - z_1)\,\vec{k} \tag{10}$$

$$\Delta\vec{r} = \Delta x\,\vec{i} + \Delta y\,\vec{j} + \Delta z\,\vec{k} \tag{11}$$

The unit vector $\vec{u}_r$ showing the direction of the displacement vector is obtained by Equation (12).

$$\vec{u}_r = \frac{\Delta\vec{r}}{\left|\Delta\vec{r}\right|} = \frac{\Delta\vec{r}}{\sqrt{(\Delta x)^2 + (\Delta y)^2 + (\Delta z)^2}} \tag{12}$$

If the total path between A and B is divided into N segments, the 3D coordinates of the initial and final points of the kth segment are calculated by Equations (13) and (14), respectively. The indices i and f used in these equations represent the initial and final points of the kth segment.

$$x_{k-i}\,\vec{i} + y_{k-i}\,\vec{j} + z_{k-i}\,\vec{k} = \left(x_1\,\vec{i} + y_1\,\vec{j} + z_1\,\vec{k}\right) + \vec{u}_r\left(\frac{\left|\Delta\vec{r}\right|}{N}(k-1)\right) \tag{13}$$

$$x_{k-f}\,\vec{i} + y_{k-f}\,\vec{j} + z_{k-f}\,\vec{k} = \left(x_1\,\vec{i} + y_1\,\vec{j} + z_1\,\vec{k}\right) + \vec{u}_r\left(\frac{\left|\Delta\vec{r}\right|}{N}k\right) \tag{14}$$

Knowing the coordinates of all of the measurement spots, the angles α and β can be calculated for all intermediate points and then used to decompose the recorded vibration response into the corresponding axes.

While performing dynamic tests on large structures, temperature variations and other similar environmental factors may affect the obtained modal parameters, even if there is no damage [36,37]. This may cause some false alarms and difficulties in interpreting the obtained results. Specifically, the response characteristics of steel structures change significantly depending on the ambient temperature. In this work, the validation tests were performed in the lab, and environmental factors were kept unchanged during the measurements. Moreover, the test model was made of wood and had relatively low sensitivity to temperature variations. Therefore, the possible effects of external factors

were expected to be negligible. However, for future studies conducted on existing large structures, the possible effects of environmental factors on dynamic response characteristics should definitely be considered.

Two alternatives may provide useful information for analyzing the acquired data and for interpreting the obtained results. First, environmental conditions and ambient temperature can be recorded in detail during the measurement campaign. Such an approach makes it possible to create a database that clearly shows how the modal parameters change depending on uncontrollable external factors. However, such an approach requires the long-term monitoring of the structure through a time period that includes daily, seasonal, and yearly fluctuations.

As an alternative approach, some advanced optimization techniques can be utilized to test the stability of the calculated dynamic properties and the reliability of the estimations. For example, swarm intelligence optimization is a newly emerging method widely applied in structural health monitoring to validate the effectiveness of analyses [38,39]. Although the current work does not include such an assessment, for possible long-term tests and analyses performed on large structures, evaluating the reliability of the damage estimations determined by these optimization techniques is at the center of our future research plans.

7. Conclusions

Within the scope of this work, an innovative structural health monitoring system was proposed for the rapid assessment of the current health/damage condition of high-rise buildings, large-sized chimneys, bridges, and similar facilities. Different aspects of the system, such as the measurement system and utilized data processing approach, were discussed throughout the article.

Ground-based high-resolution IR infrared laser vibrometer(s) were used to measure the dynamic response of structures. A new targeting and control mechanism was developed to utilize these devices as automated scanners in a fast and efficient way. A different methodology was followed to overcome difficulties in guiding IR laser systems.

The laser source was fixed on a platform that can rotate about two axes simultaneously, and it was targeted towards the desired spot by moving the platform rather than by directing the beam using mirrors and lenses. The proposed solution enabled high-resolution IR scanners to be designed. Since IR lasers reflect off most surfaces with a very high intensity, very accurate measurements are taken from the structure without needing to enhance its surface. Therefore, the proposed system can be applied to existing structures efficiently and with a very high accuracy and spatial resolution. Feasibility tests show that the new scanner can be programmed to test structures with intricate geometries within very short durations of 10–15 min. The cumulative measurement error is in the range of 0.06% of the dimensions of the scanned area.

Within the framework of this project, a new and modified approach that can easily be applied to finite element models is introduced. When only used for damage localization, the method does not involve the use of a finite element model. Depending on the spatial resolution of the measurements, the location of the flaw is determined precisely by comparing the experimentally obtained mode shapes. However, if present, a finite element model makes it possible to compute the extent of the flaw very accurately.

Numerical simulations performed on the FE model of a 15-story building show that the stiffness losses due to damage can be identified very precisely. The maximum error rate was in the range of 3–4%. The proposed methodology made it possible to superimpose the effects of flaws that were observed in different parts of the structure simultaneously. The instantaneous health condition of each floor was analyzed individually by decomposing a single mode shape. In this way, highly complex damage scenarios representing concurrent damage at several points of the structure can be analyzed, and damage characteristics extracted with very high mathematical and spatial accuracy.

The health monitoring system developed in this work can be applied to existing structures very efficiently. A single system can be used for the regular survey and control of

several buildings successively. Compared to conventional sensor technologies, the obtained spatial resolution is much higher. High-resolution measurements made it possible to detect the location of the flaws rapidly and allows the required precautions to be taken.

Funding: This research received no external funding.

Institutional Review Board Statement: Not applicable.

Informed Consent Statement: Not applicable.

Conflicts of Interest: The authors declare no conflict of interest.

Abbreviations

The following abbreviations are used in this manuscript:

LDV	laser Doppler vibrometer
IR	infrared
FE	finite element
MDOF	multi-degree-of-freedom
RA	relative angle

References

1. Sivasuriyan, A.; Vijayan, D.S.; Górski, W.; Wodzyń, Ł.; Vaverková, M.D.; Koda, E. Practical implementation of structural health monitoring in multi-story buildings. *Buildings* **2021**, *11*, 263. [CrossRef]
2. Harirchian, E.; Lahmer, T.; Buddhiraju, S.; Mohammad, K.; Mosavi, A. Earthquake safety assessment of buildings through rapid visual screening. *Buildings* **2020**, *10*, 51. [CrossRef]
3. Duvnjak, I.; Klepo, I.; Serdar, M.; Damjanović, D. Damage assessment of reinforced concrete elements due to corrosion effect using dynamic parameters: A review. *Buildings* **2021**, *11*, 425. [CrossRef]
4. Fradelos, Y.; Thalla, O.; Biliani, I.; Stiros, S. Study of lateral displacements and the natural frequency of a pedestrian bridge using low-cost cameras. *Sensors* **2020**, *20*, 3217. [CrossRef]
5. Kaloop, M.R.; Elbeltagi, E.; Hu, J.W. Estimating the dynamic behavior of highway steel plate girder bridges using real-time strain measurements. *Appl. Sci.* **2020**, *10*, 4215. [CrossRef]
6. Dolinski, L.; Krawczuk, M. Analysis of modal parameters using a statistical approach for condition monitoring of the wind turbine blade. *Appl. Sci.* **2020**, *10*, 5878. [CrossRef]
7. Chakraborty, J.; Wang, X.; Stolinski, M. Damage detection in multiple RC structures based on embedded ultrasonic sensors and wavelet transform. *Buildings* **2021**, *11*, 56. [CrossRef]
8. Borate, P.; Wang, G.; Wang, Y. Data-Driven Structural Health Monitoring Approach Using Guided Lamb Wave Responses. *J. Aerosp. Eng.* **2020**, *33*, 04020033. [CrossRef]
9. Sivasuriyan, A.; Vijayan, D.S.; Leemarose, A.; Revathy, J.; Gayathri Monicka, S.; Adithya, U.R.; Jebasingh Daniel, J. Development of Smart Sensing Technology Approaches in Structural Health Monitoring of Bridge Structures. *Adv. Mater. Sci. Eng.* **2021**, *2021*, 2615029. [CrossRef]
10. Capanna, I.; Cirella, R.; Aloisio, A.; Di Fabio, F.; Fragiacomo, M. Operational modal analysis and non-linear dynamic simulations of a prototype low-rise masonry building. *Buildings* **2021**, *11*, 471. [CrossRef]
11. Zabielski, J.; Srokosz, P. Monitoring of structural safety of buildings using wireless network of mems sensors. *Buildings* **2020**, *10*, 193. [CrossRef]
12. Bianchi, S.; Biondini, F.; Rosati, G.; Anghileri, M.; Capacci, L.; Cazzulani, G.; Benedetti, L. Structural Health Monitoring of Two Road Bridges in Como, Italy. *Lect. Notes Civil Eng.* **2022**, *200*, 45. [CrossRef]
13. Bertolesi, E.; Buitrago, M.; Adam, J.M.; Calderón, P.A. Fatigue assessment of steel riveted railway bridges: Full-scale tests and analytical approach. *J. Constr. Steel Res.* **2021**, *182*, 106664. [CrossRef]
14. Li, S.; Wang, X.; Liu, H.; Zhuo, Y.; Su, W.; Di, H. Dynamic deflection monitoring of high-speed railway bridges with the optimal inclinometer sensor placement. *Smart Struct. Syst.* **2020**, *26*, 591–603. [CrossRef]
15. Kaur, G.; Kaler, R.S. Investigate the optical FBG sensor to monitor displacement and vibration in civil structure. *Opt. Quantum Electron.* **2022**, *54*, 121. [CrossRef]
16. Li, T.; Wu, D.; Khyam, M.O.; Guo, J.; Tan, Y.; Zhou, Z. Recent Advances and Tendencies regarding Fiber Optic Sensors for Deformation Measurement: A Review. *IEEE Sens. J.* **2021**, *22*, 91. [CrossRef]
17. Nong, S.; Yang, D.; Yi, T. Pareto-based bi-objective optimization method of sensor placement in structural health monitoring. *Buildings* **2021**, *11*, 549. [CrossRef]
18. Afrouz, S.G.; Razavi, M.R.; Pourkand, A.; DiasWilson, C.M. Dynamic displacement of an aluminum frame using close range photogrammetry. *Buildings* **2019**, *9*, 176. [CrossRef]

19. Rinaldi, C.; Ciambella, J.; Gattulli, V. Image-based operational modal analysis and damage detection validated in an instrumented small-scale steel frame structure. *Mech. Syst. Signal Processing* **2022**, *168*, 108640. [CrossRef]
20. Helming, P.; Von Freyberg, A.; Sorg, M.; Fischer, A. Wind turbine tower deformation measurement using terrestrial laser scanning on a 3.4 MW wind turbine. *Energies* **2021**, *14*, 3255. [CrossRef]
21. Zieger, T.; Nagel, S.; Lutzmann, P.; Kaufmann, I.; Ritter, J.; Ummenhofer, T.; Knodel, P.; Fischer, P. Simultaneous identification of wind turbine vibrations by using seismic data, elastic modeling and laser Doppler vibrometry. *Wind Energy* **2020**, *23*, 1145–1153. [CrossRef]
22. Spanos, N.A.; Sakellariou, J.S.; Fassois, S.D. Vibration-response-only statistical time series structural health monitoring methods: A comprehensive assessment via a scale jacket structure. *Struct. Health Monitor.* **2020**, *19*, 736–750. [CrossRef]
23. Poozesh, P.; Sabato, A.; Sarrafi, A.; Niezrecki, C.; Avitabile, P.; Yarala, R. Multicamera measurement system to evaluate the dynamic response of utility-scale wind turbine blades. *Wind Energy* **2020**, *23*, 1619–1639. [CrossRef]
24. Ozbek, M.; Rixen, D.J. Operational modal analysis of a 2.5 MW wind turbine using optical measurement techniques and strain gauges. *Wind Energy* **2013**, *16*, 367–381. [CrossRef]
25. Shao, Y.; Li, L.; Li, J.; An, S.; Hao, H. Computer vision based target-free 3D vibration displacement measurement of structures. *Eng. Struct.* **2021**, *246*, 113040. [CrossRef]
26. Wu, T.; Tang, L.; Shao, S.; Zhang, X.-Y.; Liu, Y.-J.; Zhou, Z.-X. Cost-effective, vision-based multi-target tracking approach for structural health monitoring. *Meas. Sci. Technol.* **2021**, *32*, 25116. [CrossRef]
27. Dilek, A.U.; Oguz, A.D.; Satis, F.; Gokdel, Y.D.; Ozbek, M. Condition monitoring of wind turbine blades and tower via an automated laser scanning system. *Eng. Struct.* **2019**, *189*, 25–34. [CrossRef]
28. Chinka, S.S.B.; Putti, S.R.; Adavi, B.K. Modal testing and evaluation of cracks on cantilever beam using mode shape curvatures and natural frequencies. *Structures* **2021**, *32*, 1386–1397. [CrossRef]
29. Gorgin, R.; Wang, Z. Structural damage identification based on principal curvatures of mode shape. *Int. J. Acoust. Vib.* **2021**, *25*, 566–576. [CrossRef]
30. O'Shea, M.; Murphy, J. Design of a BIM integrated structural health monitoring system for a historic offshore lighthouse. *Buildings* **2020**, *10*, 131. [CrossRef]
31. Ereiz, S.; Duvnjak, I.; Damjanović, D.; Bartolac, M. Analysis of seismic action on the tie rod system in historic buildings using finite element model updating. *Buildings* **2021**, *11*, 453. [CrossRef]
32. Ozbek, M.; Rixen, D.J. A new analysis methodology for estimating the eigenfrequencies of systems with high modal damping. *J. Sound Vib.* **2016**, *361*, 50. [CrossRef]
33. Meng, F.; Ozbek, M.; Rixen, D.J.; Van Tooren, M.J.L. Comparison of System Identification Techniques for Predicting Dynamic Properties of Large Scale Wind Turbines by Using the Simulated Time Response. In *Structural Dynamics and Renewable Energy*; Conference Proceedings of the Society for Experimental Mechanics Series; Springer: Berlin/Heidelberg, Germany, 2011; Volume 1, pp. 339–349. [CrossRef]
34. Piezoelectric Accelerometer, PCB Piezotronics. 2022. Available online: https://www.pcb.com/products?model=393B04 (accessed on 22 March 2022).
35. Long-Range Laser Doppler Vibrometer, Polytec GmbH. 2022. Available online: https://www.polytec.com/int (accessed on 22 March 2022).
36. Huang, M.; Lei, Y.; Li, X. Structural Damage Identification Based on l 1Regularization and Bare Bones Particle Swarm Optimization with Double Jump Strategy. *Math. Probl. Eng.* **2019**, *2019*, 5954104. [CrossRef]
37. Huang, M.S.; Gül, M.; Zhu, H.P. Vibration-Based Structural Damage Identification under Varying Temperature Effects. *J. Aerosp. Eng.* **2018**, *31*, 829. [CrossRef]
38. Huang, M.; Zhao, W.; Gu, J.; Lei, Y. Damage Identification of a Steel Frame Based on Integration of Time Series and Neural Network under Varying Temperatures. *Adv. Civil Eng.* **2020**, *2020*, 4284381. [CrossRef]
39. Wang, Z.; Huang, M.; Gu, J. Temperature effects on vibration-based damage detection of a reinforced concrete slab. *Appl. Sci.* **2020**, *10*, 2869. [CrossRef]